A quantitative study of thermal cycling along the build direction of Ti-6Al-4V produced by laser powder bed fusion

Ming Chen[1], Marco Simonelli[2], Steven Van Petegem[1,], Yau Yau Tse[3], Cynthia Sin Ting Chang[4], Malgorzata Grazyna Makowska[1,5], Dario Ferreira Sanchez[5], Helena Moens-Van Swygenhoven[1,*]*

1. Photon Science Division, Paul Scherrer Institut, Forschungsstrasse 111, 5232 Villigen PSI, Switzerland

2. Centre for Additive Manufacturing, University of Nottingham, UK

3. Department of Materials, Loughborough University, UK

4. Technology Transfer Centre for Advanced Manufacturing, ANAXAM, PARK INNOVAARE: deliveryLAB, 5232 Villigen PSI, Switzerland

5. MicroXAS Beamline, Paul Scherrer Institut, Forschungsstrasse 111, 5232 Villigen PSI, Switzerland

*Corresponding authors:

steven.vanpetegem@psi.ch, helena.vanswygenhoven@psi.ch

Highlights

- High-speed *in situ* X-ray diffraction during laser scanning were performed on a Ti-6Al-4V thin wall produced by laser powder bed fusion.

- The temperature evolution and cooling rates were determined as a function of depth with a time resolution of 50 μs.

- Based on the evolution of the crystallographic phases the shape of the melt pool and the β phase in the heat-affected zone could be estimated.

- The depth-dependent temperature profiles provide valuable input for the calibration of finite element simulations

Abstract

During laser-powder bed fusion (L-PBF) the printed material is subjected to multiple fast heating and cooling cycles when the laser interacts with neighboring tracks or layers above. The complex thermal history influences the final microstructure and the macroscopic properties of the printed part. In this work, we demonstrate how high-speed *in situ* X-ray diffraction in transmission mode can be used to measure temperature profiles and cooling rates in a Ti-6Al-4V single-track wall. During the laser remelting of the top layer, a temperature exceeding the β transus temperature ($T_\beta \sim$ 1252 K) is measured up to 150 μm below the surface. The maximum observed cooling rates vary from 10^6 K/s at the top surface, to 10^5 K/s at a depth of 135 μm and 10^4 K/s at a depth of 255 μm. Based on the temporal evolution of the various crystallographic phases, the dimensions of the melt pool and the high-temperature β zone surrounding the melt pool are estimated. It is anticipated that the data obtained from *in situ* measurements in transmission mode on a thin wall combined with *in situ* measurements in reflection mode on a bulk sample will allow verification and validation of finite element models used in L-PBF processing.

Keywords: laser powder bed fusion, *in situ* X-ray diffraction, Ti-6Al-4V, thermal cycling, cooling rates

1. Introduction

Ti-6Al-4V alloys produced by laser powder bed fusion (L-PBF) typically exhibit hierarchical martensite microstructures consisting of martensitic alpha prime (α′) laths encased within vertically oriented prior-β grains [1,2]. Several thermomechanical [3–7] and thermokinetic [8,9] finite-element models (FEM) have been developed to simulate and predict melt pool geometries, residual stress [10–12], porosity [13,14], and microstructures [15–17] produced by L-PBF. During the manufacturing process, the deposited material is subjected to multiple thermal cycles, both when the laser interacts with neighboring tracks belonging to the same layer and when successive layers are progressively deposited. Thermal cycles can be considered as a series of fast intrinsic heat treatments that gradually develop the microstructure causing phase decomposition, elemental partitioning and defect evolution [18]. Therefore, thermal cycling is expected to influence the microstructures and residual stresses in Ti alloys [4,8,19,20] and the resulting mechanical properties [21–23].

A qualitative model of thermal cycling has been proposed in the literature to support the interpretation of the observed hierarchical martensites in printed Ti-6Al-4V [24,25]. The development of such a model would benefit from more accurate information on the geometry and temperatures of the heat-affected zone (HAZ) during thermal cycling. Thus, it is essential to measure the temperature profiles and phase transformation (β→α') during the manufacturing process.

During past years, several in situ synchrotron X-ray diffraction and imaging experiments have been performed to study the microstructure evolution during metal 3D printing. The melt pool dynamics can be studied in detail by fast radiography experiments [26–31]. The evolution of the crystallographic phases, stress and temperature has been investigated by in situ X-ray diffraction [28,32–35]. High-speed X-ray imaging and diffraction experiments in transmission mode have been conducted to monitor phase transformation in Ti-6Al-4V during laser scanning [36,37]. High-speed in situ X-ray diffraction in reflection mode has been used to measure the local temperature and cooling rates in the upper layer during printing a 3D Ti-6Al-4V structure [38,39]. These results have been used to evaluate different heat source models in FEM simulations, [39]. For instance, FEM simulations using a single ellipsoid model consisting of a volumetric Gaussian heat flux derived from the double ellipsoid model of Goldak [3,5], provide similar values as the cooling rates and melt

pool dimensions measured at the sample surface during *in situ* X-ray diffraction [39]. Heat models considering a cylindrical heat flux with parabolic decay for penetration [10] performed better in the depth and width, but the melt pool length on the surface of the sample is considerably smaller. The temperature profiles of layers below the top surface plane are however more difficult to measure. Thermocouples would be a natural choice [19,40], however, these can only be inserted at a sufficient distance to the melt pool to avoid high-temperature damage.

A systematic study of thermal profiles along the building direction during layer-by-layer deposition is essential to quantify the thermal cycling effect. It is also indispensable to verify and calibrate existed heat sources models for FEM in order to increase their accuracy. However, the direct measurement of temperatures data at different distances from the laser processing surface is rather limited, especially at regions close to melt pool. In this study, we propose a method to obtain the temperature profiles below the processing plane during L-PBF by using high-speed *in situ* X-ray diffraction in transmission mode while the laser re-scans the top of a previously printed thin wall. We apply this method to Ti-6Al-4V, a representative alloy widely used in L-PBF process. The phase evolution, temperature profile, and cooling rates were measured for different layers every 30 µm, corresponding to the nominal layer thickness of printed the wall, with a high time resolution of 50 µs. The temperature profiles and phase evolution as a function of time were used to estimate the dimensions of the melt pool and the β zone surrounding the melt pool. We advocate that the data obtained from *in situ* measurements in transmission mode on a thin wall combined with *in situ* measurements in reflection mode on a bulk sample allows full verification and validation of finite element L-PBF models.

2. Materials and methods

2.1. Powder feedstock

The powder used in this study was a pre-alloyed Ti-6Al-4V powder, produced by plasma atomization and supplied by LPW Technology (now Carpenter Additive, USA). The spherical morphology of the Ti-6Al-4V powder is shown in the backscattered electron micrographs Fig. S1 in Supplementary Materials. The particle size distribution was measured by a laser diffraction particle size analyzer Partica LA-950 V2 system

(Horiba, Tokyo, Japan). The size distribution is as follows: D_{10} = 21.8 μm, D_{50} = 33 μm and D_{90} = 49.5 μm.

2.2. Single-track wall manufactured by laser powder bed fusion

Prior to the *in situ* X-ray diffraction experiments, a single-track wall was printed with a miniaturized L-PBF printer. Details on this setup can be found in Refs. [38,41]. Table 1 summarizes the most important process parameters. During printing, the process chamber was continuously flushed with high purity Ar, to keep the oxygen levels well below 0.2%. A Ti-6Al-4V thin wall with approximate dimensions of 6 mm length, 1.2 mm height and 0.1 mm thickness was printed by stacking 40 single tracks. After printing, the loose powder around the walls was gently removed. A schematic view of the printed thin wall is shown in Fig. 1a. The layers are numbered from L1 to L40 with L1 being the last printed layer.

Table 1. Overview of the process parameters used for printing a single-track wall.

Laser spot size	100 μm
Laser power	200 W
Scan speed	600 mm/s
Nominal layer thickness	30 μm
Base plate material	Ti-6Al-4V
Base plate temperature	Ambient temperature

2.3. *In situ* X-ray diffraction measurement

In situ X-ray diffraction experiments were performed while the laser rescanned the top surface of the printed wall. This was conducted using the same miniaturized L-PBF printer, mounted at the MicroXAS beamline located at the Swiss Light Source. A schematic of this *in situ* experiment is shown in Fig. 1a. The X-ray beam had an energy of 14.55 keV and a full-width at one-tenth maximum (FWTM) spot size of 110 x 30 μm^2 (width x height). The printer was tilted by 5 degrees towards the direction of the incident X-ray beam, allowing easier positioning of the X-ray beam at various heights from the top (L1) to the bottom (L40) of the wall. The volume illuminated by the X-ray

5

beam on the wall, defined as V_{XR}, has the following dimensions: 100 x 110 x 30 μm^3 labelled in Fig. 1a. A fast EIGER 1M detector [42] recorded 2D diffraction patterns at a frame rate of 20 kHz for a total duration of 1 sec. The 2D diffraction images are reduced to conventional 1D diffraction patterns by azimuthal integration using pyFAI, an established python library for fast powder integration [43].

Prior to the *in situ* experiments, the position of the top edge of the walls was determined by scanning the X-ray beam across the sample height while recording the transmission signal. For the first in situ experiment, the X-ray beam was positioned in the centre of the length of the sample at a distance of 15 μm below the top edge, i.e. the middle of the first 30 μm thickness (L1). Note that the notation L1 refers to the first 30 μm of deposited materials measured by the X-ray beam. Whilst recording transmission diffraction patterns at 20 kHz, the top layer was remelted with the same laser parameters used to build the walls (see Tab. 1). For the second in situ experiment, the centre of the X-ray beam was positioned 30 μm lower in the middle of the next layer (L2) while the top layer was remelted again. This process was repeated until L20, where V_{XR} is located at 615 μm from the top edge of the wall. There was sufficient time between each remelt for the complete wall to cool down to room temperature. It is worth noting, as one major difference to normal L-PBF, these *in situ* experiments were performed by melting directly the same top layer (L1) without adding fresh loose powders. In other words, layer L1 was remelted N times, while diffraction patterns were recorded at layer L_N. It is known that the laser absorption coefficient of a solid layer (~0.3) [11] is lower than that of a powder layer (0.3−0.6) [7,44]. This difference is also influenced by laser wavelength [45,46] and the roughness of solid surface [47]. It can be assumed that the temperature evolution measured in the present experiments should not deviate significantly from those during printing. In addition to the *in situ* measurements, spatially resolved X-ray diffraction was performed before and after 20 times remelting to determine the microstructure with better statistics. For each layer, 50 diffraction patterns were acquired along a horizontal line with a step size of 0.1 mm and then summed up.

2.4. Phase identification and temperature calculation

Analysis of the diffraction patterns was performed with in-house written MATLAB routines. Fig. 1b displays exemplary diffraction intensity versus diffraction angle as a

function of time acquired with V_{XR} positioned on layer L1. The t = 0 ms is defined as the moment when the laser passes through V_{XR} with a temperature increase of 5% above ambient temperature. The exact procedure is described in detail in Supplementary Materials (Fig. S2). Fig. 1c shows the diffraction patterns at three characteristic times. Prior to laser melting (t < 0 ms), the diffraction patterns exhibit only peaks from the hexagonal close-packed (hcp) α/α' phase. Note that both α and α' phases are expected to form because of the high cooling rates during printing and remelting. The α and α' phases share the same hcp structure and exhibit similar lattice parameters with a small difference [48]. It is difficult to differentiate them in the X-ray diffraction patterns from the high-speed *in situ* measurements. Therefore, the peaks from the hcp structure are referred to as α/α'. When the laser passes through V_{XR}, the sharp hcp diffraction peaks completely disappear. The diffraction pattern now reflects the presence of the liquid phase with typical low reflection intensity [49], as shown in Fig. 1c at t = 0.25 ms. The remaining weak peaks can be assigned to diffraction of non-molten solid located outside the melt pool but inside V_{XR}. Starting from t = 0.3 ms, the diffracted peaks of the high-temperature β phase grow and reach their maximum at t = 1.05 ms (see Fig. 1c). The layers L2 and L3 exhibit similar behaviour, as shown in Fig. S3 in Supplementary Materials. The liquid fraction is lower in L2 and L3, as shown by the larger intensities of the remaining diffraction peaks of the solid phase. Layer L4 and the layers below did not show any sign of a molten phase.

During heating and cooling, the diffracted peaks shift from the positions recorded at ambient temperature. Assuming that the peak shift is entirely due to isotropic thermal expansion, temperatures of the solid phases can be derived. The elastic strain of the crystalline lattice induced by the thermal expansion or contraction is determined by the relative shift of the peak positions (2θ). To calculate the lattice strain, a reference lattice parameter of 0.3246 nm for β phase [34,50] and lattice parameters of 0.2938 and 0.4668 nm for *a* and *c* of hcp α' phase [24] are used. The lattice strain prior to remelting is very similar in all layers and amounts to 0.04 ± 0.02%. This lattice strain, in turn, is used to calculate the local temperature in V_{XR} by applying the temperature-dependent thermal expansion coefficients [51]. The detailed calculation procedure and formulas can be found in Ref [41]. During the martensitic phase transformation, the β phase experiences significant tensile stresses [38]. Therefore, the temperature profiles are only measured until that point. Since heating and cooling rates are quite fast, the

diffraction patterns recorded with the high frame rate of 20 kHz can be noisy at the onset of a phase transformation. We identify the martensite start temperature M_s^X when the integrated intensity of {01.1} α/α' reflection peaks exceeds 1 count per pixel after background subtraction. Below this threshold, the noise level is too high, resulting in large temperature fluctuations. A similar criterion is applied for the β phase, where the temperature is derived from the {011}β reflection. The martensite finish temperature M_f^X is identified when the integrated intensity of the β phase is lower than 1 count per pixel. The findings will be discussed with respect to literature reference values for the β transus ($T_β$) ~1252 K, M_s ~1053.15 K, and M_f ~923.15 K for Ti-6Al-4V [52]. Note that important temperature gradients can be present in the volume V_{XR} (100 x 110 x 30 μm^3), especially at high temperatures, hence the measured temperature values are an average over this volume. The magnitude of the temperature gradient within V_{XR} and the sources that may contribute to errors in temperature calculation are discussed in Section 4.
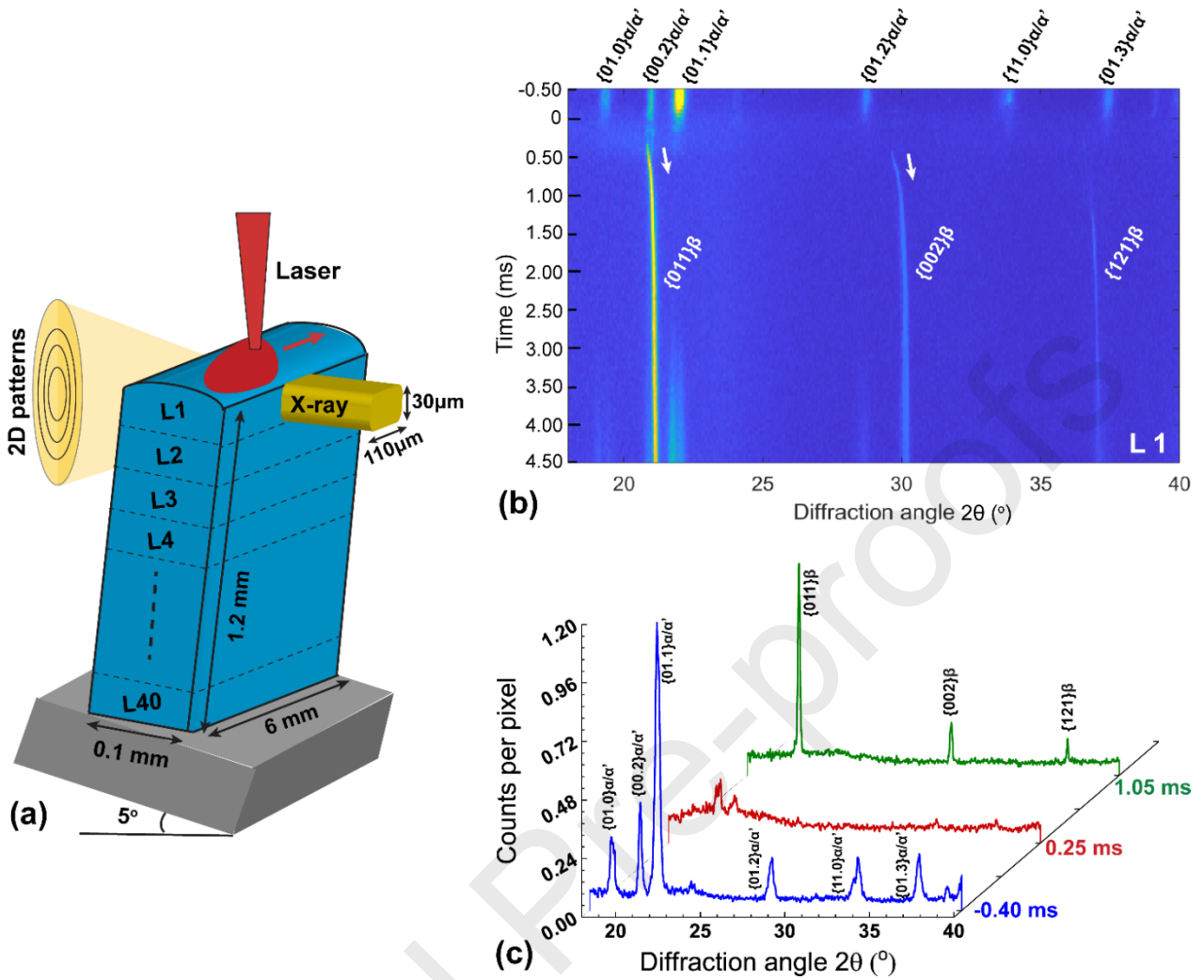
Figure. 1 Demonstration of the in situ X-ray diffraction measurement. (a) Schematic of the in situ experiment with a focused X-ray beam positioned at the top layer of a Ti-6Al-4V wall (denoted as L1). (b) Evolution of the diffraction patterns as a function of time measured with the X-ray beam positioned at the L1 during laser scanning. The colour scale is cut at 0.8 counts per pixel to optimize visibility. (c) Single diffraction patterns recorded prior to heating (t = -0.40 ms), at the molten state (t = 0.25 ms), and during cooling (t = 1.05 ms), showing the phase transformation between the liquid and solid phases of Ti-6Al-4V.

2.5. Microstructure characterization

The microstructure of the Ti-6Al-4V wall cross-section was analyzed by scanning electron microscopy (SEM). Electron backscatter diffraction (EBSD) was performed in a Helios plasma focused ion beam (ThermoFisher Scientific) equipped with a symmetry EBSD detector using an electron beam operated at 20 keV. EBSD maps

are obtained using 0.2 µm step size for scanning the whole wall and 0.1 µm step size in a high-resolution scan for L1, L3, and L7. Post-processing of EBSD data and map construction was done with the HKL-Channel 5 TM.

3. Results

3.1. Phase transformations induced by the intrinsic heat treatments during the L-PBF process

The results of *in situ* X-ray diffraction from layers L1−L6 of the wall are shown in Fig. 2. The first column of Fig. 2 (a, d, g, j, m, and p) shows the integrated intensities of the $\{01.1\}\alpha/\alpha'$ and $\{011\}\beta$ reflections as a function of time. This reflects the evolution of α/α' and β phases measured in V_{XR} for each layer during the passage of the laser on the different layers. The second column in Fig. 2 (b, e, h, k, n, and q) shows the temperatures measured in the V_{XR}, which are derived from the peak shifts of the $\{01.1\}\alpha/\alpha'$ and $\{011\}\beta$. The third column of Fig. 2 (c, f, i, l, o, and r) shows a schematic to demonstrate the position of V_{XR} relative to the melting pool at an arbitrary instant t= 2.5 ms and the estimated shape of the β phase zone and the melt pool.

The first row of Fig. 2 shows the phase evolution and the temperature profiles experienced in V_{XR} positioned in L1 as the laser approaches, traverses, and leaves this probed volume. As the laser approaches V_{XR}, the material heats up much more rapidly than the detection rate and as a result, only a limited portion of the heating ramp can be captured. Fig. 2a shows that at t = 0.2 ms, intensities of both phases vanish. This defines the onset of melting of V_{XR}. Neglecting weak reflection intensities (as shown in the diffraction pattern at t = 0.25 ms in Fig. 1c), the total time that V_{XR} remains in the molten state is estimated as 0.4 ms. By considering the laser scanning speed of 600 mm/s and the actual width of the X-ray beam (~110 µm), the melt pool is estimated to have a total length of 350 µm (as outlined in detail in the Supplementary Materials Fig. S4). Its width corresponds with the thickness of the wall (~100 µm). After 0.6 ms, the β phase appears at T = 1907 K meaning that the width of the melt pool is now smaller than the thickness of the wall, and a mixture of liquid and solid β phase is measured over a length of 160 µm (Fig. S4a). Then V_{XR} solidifies entirely into the β phase, the $\{011\}\beta$ reflection achieves the maximum integrated intensity of 7.3 counts per pixel at t = 1.05 ms, at which a temperature of 1362 K is measured. The β region

has a thickness inferior to that of V_{XR} over a length of 1400µm. Fig. 2c schematically shows the relative position of the heat-affected zone (HAZ) and V_{XR} in L1 at t = 2.5 ms. At t = 3.2 ms (T= 988 K), the solid phase transformation (β → α') starts in the cooler regions at the surfaces of V_{XR} until approximately t = 4 ms corresponding to T= 943 K. This indicates a length of the tail part of mixture region of β and α' phases is about 370 µm. The temperatures calculated from both phases overlap quite well around this time with only a small deviation of about 30 K (Fig. 2b), which can be attributed to the fact the calculated temperature is an average value from the whole V_{XR}.

The thermal cycle imposed by L-PBF when V_{XR} is positioned in the centre of L2 is shown in Figs. 2d−2f. When the laser approaches, V_{XR} is rapidly heated and only partly molten at t= 0.5 ms, as suggested by the presence of remaining diffraction peaks (see Fig. S3a in Supplementary Materials). As the laser leaves V_{XR}, the β phase is detected at t = 0.7 ms (T = 1655 K) and then achieves the maximum intensity at t= 1.1 ms. The V_{XR} probes only the β phase until t = 2.3 ms. This corresponds to a maximum length of the complete β phase zone of 830 µm. The α/α' phase is present from t = 2.3 ms, at a temperature of T= 970 K. Both phases co-exist for approximately 1.7 ms until t = 4 ms, resulting in a maximum length of β region including its tail part in the HAZ of 1740 µm. Beyond t = 4 ms, V_{XR} exhibits a single α/α' phase while cooling to ambient temperature.

The phase and temperature evolution when V_{XR} is positioned in the centre of L3 is shown in Figs 2g−2i. The thermal cycle is for the most part analogous to that experienced by L2. Only the upper part of V_{XR} transforms into liquid at t = 0.2 ms, as suggested by the reduced intensities of the diffraction peaks (at t = 0.2 and 0.25 ms, Supplementary Materials Fig. S3d). This suggests that the depth of the melt pool is of the order of 75 µm, as schematically depicted in Fig. 2i. The V_{XR} probes the β phase between t = 0.45 ms and t = 2.45 ms, the maximum intensity is reached at t = 1 ms. This means that the β region covers the full thickness of the wall over 980 µm. The {01.1}α/α' reflection is present at t = 2.45 ms, i.e. T = 979 K. Both α' and β phases co-exist for approximately 0.55 ms until t = 3 ms (T= 924K). The maximum length of the β zone including the tail (where both solid phases are present) amounts to 1200 µm. As shown in Fig. 2i, at t= 2.5 ms, V_{XR} is located at the boundary of α/α' and β zones.

So the thermal cycle experienced by L3 is mostly a rapid heat treatment to the β phase, followed by quenching.

When V_{XR} is positioned at layer L4, the material is rapidly heated from T= 1280 K at t = 0.5 ms to a maximum temperature of T = 1380 K at t= 0.75 ms, where α/α' and β coexist (Fig. 2k). The β phase achieves maximum intensity at t = 0.75 ms (T= 1380 K) and then disappears at t = 2.95 ms (T= 934 K). The maximum length of the β zone including its tail amounts to 1320 µm. At t = 2.5 ms the intensity of the {01.1}α/α' reflection is higher than that of {011}β, suggesting that at that time, V_{XR} has to a great part cooled down into the α/α' phase, as is shown in Fig. 2l. Note that between t=0.75 ms and t = 2.95 ms, there is a slight disparity between the measured temperatures of both phases. This is because within V_{XR} the two phases are spatially separated, schematically represented in Fig. S6 in Supplementary Materials. The inner β phase has a slightly higher temperature compared to the outer α/α' phase. The thermal cycle experienced by L4 is therefore equivalent to a rapid heat treatment into the α+β phase, followed by quenching.

The fifth layer (L5) below the processing plane experiences a heat treatment that still allows solid phase transformations. As the heating rate is slower, it is possible to estimate with more accuracy the temperature at which the α/α' phase starts to transform into β phase. The β phase is detected at t = 0.45 ms (Fig. 2m) with a temperature of 1360 K and heats up to a maximum temperature of 1407 K (t = 0.6 ms). During the cooling of layer L5, the β phase is cooled down to 951 K (t = 3.4 ms). The schematic in Fig. 2o shows the relative position of V_{XR} at the time t = 2.5 ms, at which the intensities of reflections from both phases are clearly probed. It is therefore possible to estimate that L5 experiences the equivalent of the rapid heat treatment in the medium portion of the α+β phase field, followed by quenching.

In the lower layers L6, L7, etc., no solid-phase transformations could be detected. Fig. 2p presents the evolution of the diffraction patterns measured when V_{XR} is positioned at approx. 150−180 µm below the top of the wall (L6) as layer L1 is melted. The material reaches a maximum temperature of T= 845 K. This is accompanied by a small decrease in the intensity of α/α' reflection due to thermal diffuse scattering. As the material cools to ambient temperature, the intensities of {01.1}α/α' reflection recover. The full temperature profiles until ambient temperature for layers L1−L10 are shown in the Supplementary Material Fig. S5.
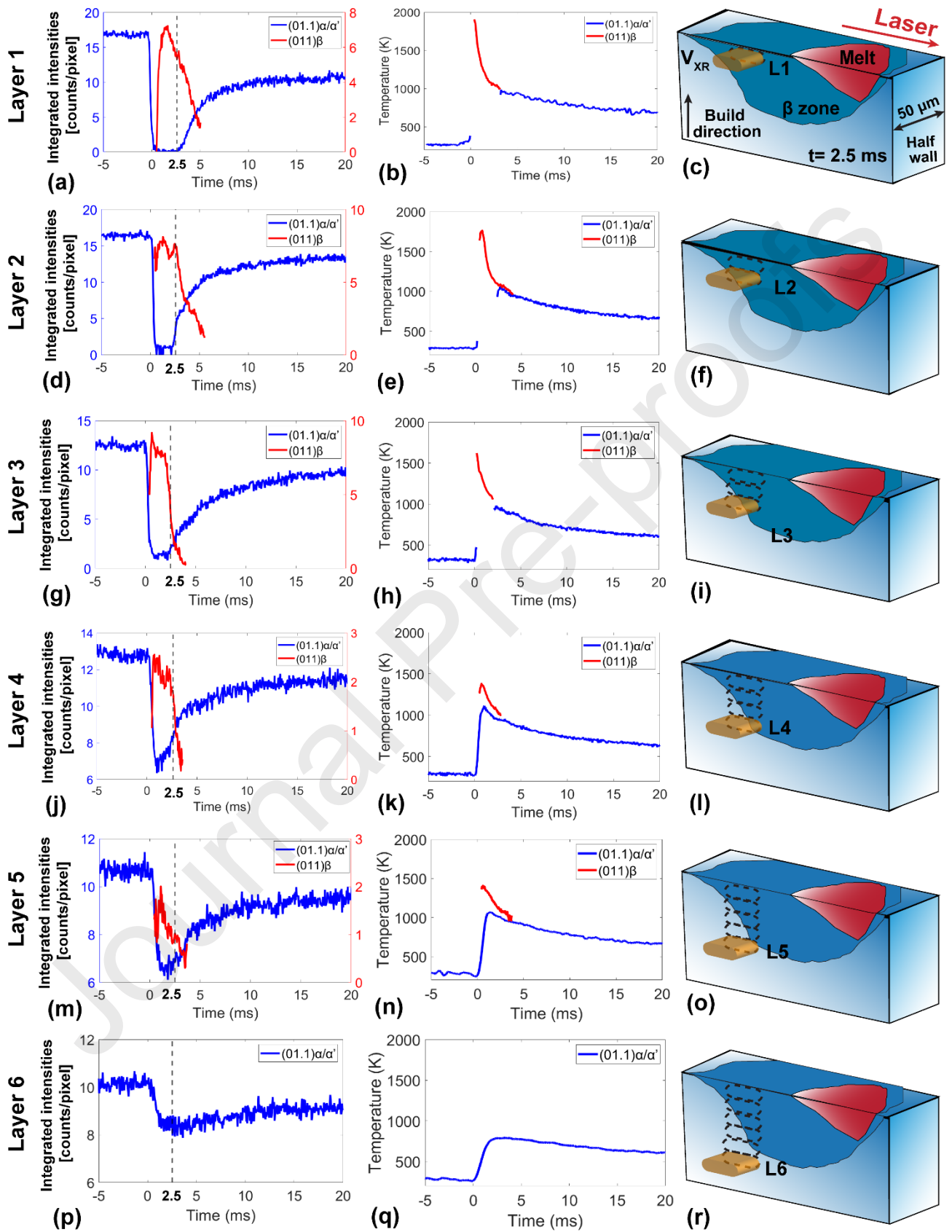
Figure 2. Thermal cycles in L1−L6 during laser remelting. The first column shows the

evolution of integrated intensities of {01.1}α/α' and {011}β reflections as a function of

13

time. The second column shows the temperatures as a function of time calculated from {011}β – red and {01.1}α/α' – blue. The third column represents a schematics of the relative positions of the volume probed by the X-ray beam V_{XR} (brown), melting pool (red), the β phase (blue), and the α' phase (white) at the cross-section of the wall for layers L1−L6 at t = 2.5 ms. The size of the melt pool and β zone along the horizontal direction are not to scale.

4. Discussion

4.1 Temperature and cooling profiles along the build direction

Using *in situ* X-ray diffraction, the temperature and cooling rates experienced by a volume V_{XR} located at different distances from the top surface of an L-PBF printed wall were measured while the upper layer was remelted. Fig. 3 shows a summary of the temperature profiles measured in L1−L6. In the first five layers (L1−L5) the maximum temperatures exceed T_{β} (~1252 K). The maximum temperatures calculated from the β phase in L4 and L5 exhibit a smaller difference than expected. This can be attributed to the strong overlap between the {011} β and the (00.2) α/α' peak at the start of the cooling, which causes some potential errors in the determination of the position of diffraction peaks. From layer L6 on, located at a depth of 150−180 μm below the top surface, the peak temperatures below T_{β} are too low to induce a phase transformation. In other words, transformations between α/α' and β phases are thought to occur predominantly in the top five layers. It is worth noting that since the *in situ* heating and cooling during thermal cycling are fairly rapid, phase transformations during L-PBF occur at significantly different temperatures compared to water quenching conditions. Table 2 summarizes the temperatures measured when the α/α' phase appears (M_s^X) in V_{XR} and the temperature when the solid phase transformation β→α' (M_f^X) is finished, using the intensity criteria specified in Section 2.4. The temperature measured for M_s^X and M_f^X are within a certain error similar for each layer. The M_s^X temperatures observed in the upper layers (L1−L3) is in the temperature range of 970−988 K. This is about 100 K lower compared to the M_s of ~1073.15 K reported under a relatively low cooling rate [52]. Although one could explain this variation as an excess of undercooling needed by the martensitic reaction to take place given the high cooling rates imposed by the process, the temperature gradients in the volume V_{XR} (due to the presence of

free surfaces of the wall) also affect the measurement of these critical temperatures, especially at high temperatures. In addition to that, the value corresponds to the temperature at which the {01.1}α/α' reflection achieves an integrated intensity above 1. This definition may induce a slight underestimation of M_s. The M_f^X, in the range of 924−951 K, is instead close to the reported value of 923 K. Since the M_f^X temperature is determined at the time when the integrated intensity of {011}β reflection decreases below the threshold value of 1, this induces a certain overestimation of M_f. It should be emphasized that experimentally determined temperature profiles should be compared with simulations of a wall structure since the presence of additional surfaces changes heat dissipation.
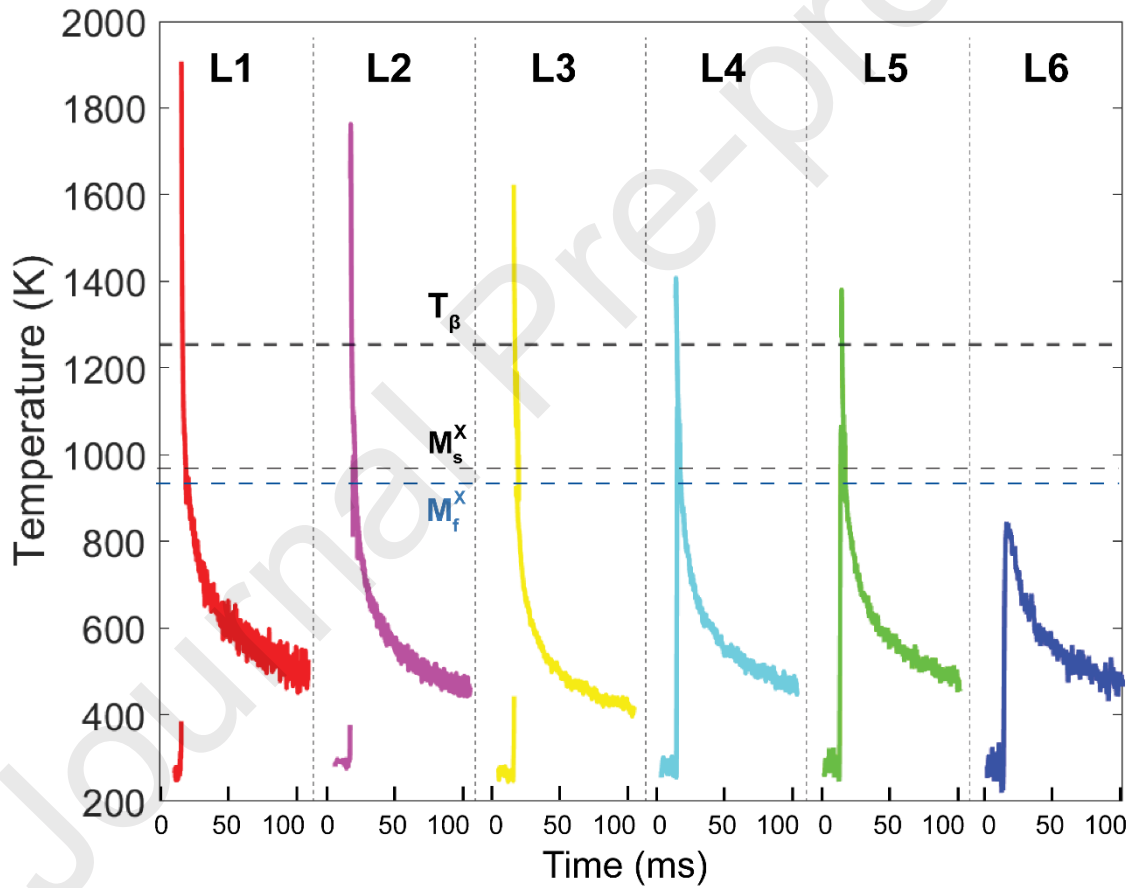

Figure 3. Temperature profiles of thermal cycles on upper layers (L1−L6) of Ti-6Al-4V wall during laser remelting on the top layer L1. The β transus ($T_β$ ~1252 K) obtained from the phase diagram of Ti-6Al-4V [52,53] and the average values of M_s^X (~979 K) and M_f^X (~937 K) measured in the present study are labelled with dashed lines.

Table 2. Summary of the temperatures measured in the different layers for the onset of α/α' phase (M_s^X) and the disappearance of the β phase (M_f^X) as measured in the upper layers during laser remelting.

Layer Num	M_s^X (K)	M_f^X (K)
L1	988	943
L2	970	935
L3	979	924
L4	--	934
L5	--	951

During laser scanning, the material experiences rapid heating and subsequent cooling. The heating rate is generally higher than the cooling rate [54]. For the upper layers of L1−L3, the heating rate is too high to be captured by the present frame rate of 20 kHz. For the lower layers L4−L10, the maximum heating rates were determined in the range of 8.5 x 10⁴ − 1.8 x 10⁶ K/s as shown in Supplementary Materials Fig. S7b. The cooling rate shows a significant dependency on the temperature in all layers. It varies between 10⁶ K/s immediately after solidification in the upper 2 layers to 20 K/s near the end of the cooling period (Fig. S7a). The cooling rate is proportional to heat flux (q) dissipation through both radiation and convection modes, which occur simultaneously during cooling but exhibit different relationships with temperature [55]. According to Stefan-Boltzmann's law, the radiation heat flux (q_{rad}) has an exponential relationship with temperature T as: $q_{rad} \propto f(T^4 - T_0^4)$. In Newton's law, the convection heat flux (q_{conv}) with surroundings has a linear relationship with temperature T as: $q_{conv} \propto f(T - T_o)$. Heat radiation loss is dominant at high temperatures, explaining the high cooling rates at high temperatures. It is worth noting that the maximum cooling rate in the top layer of the wall (~1x10⁶ K/s) is higher compared to what was obtained for the surface layer in Ti-6Al-4V bulk samples (~6.5x10⁵ K/s) [39] printed with the same laser process parameters. There are two mechanisms contributing to this difference: (1) the heat accumulation during single track printing is limited compared to multi-track printing, (2) radiation loss at high temperature is more important in the wall because of the free surfaces exposed to Ar gas flow. This result demonstrates a geometrical effect on

cooling behaviour during manufacturing. Because of the presence of free surfaces in the 2D nature of the thin wall structures, the ratio between the heat loss by radiation and convection is different. This hints for considering the effects of geometries and locations on thermal cycling during L-PBF of complex structures such as lattice and truss structures [56,57]. Below M_f, the cooling rate as a function of temperature (Fig. S7a) exhibits a change in slope (black arrow). This may be related to an increased lattice contraction during the β → α/α' transformation [50,58]. In addition, residual stresses also arise because of the difference in thermal expansion between the α/α' and β phases [11,59].

4.2 Estimation of the melt pool size and the heat-affected zone

The above results allow estimating the size and phase composition of the heat-affected zone (HAZ) induced by laser scanning. Fig. 4 shows an estimated shape of the melt pool and β zone at the cross-section in the center of the wall and perpendicular to the X-ray beam. The position of layers L1−L6 is indicated. Solid colors red and blue are used for the zones where the melt pool and the β phase respectively extend over the thickness of the wall (90−100 μm). Graded colors correspond to zones that are thinner than the wall thickness. The procedure to calculate the length of each region in L1 is detailed in Supplementary Materials Fig. S4. According to the temperature profiles and phase evolutions measured by the *in situ* experiments (Fig. 2), the melt pool covering the entire wall thickness in L1 has approximately a length of 350 μm and a depth of 75 μm. For a more accurate determination of the dimensions of HAZ, X-ray imaging methods should be applied [27,29]. SEM observations at the bottom of the wall, as shown in Fig. S11 in the Supplementary Materials, confirm the above-mentioned melt pool depth.

Assuming that the maximum intensity of the β reflection is reached at the tail of the melt pool, the total length of the melt pool including the tail surrounded by the β phase in L1 amounts to ~510 μm. There is a region of 1400 μm where the β phase covers the thickness of the wall. Thereafter, there are instants in which both the β and α/α' phases are detected. Performing a similar analysis for the other layers, a full picture of the heat-affected zone is obtained, demonstrating that the melt pool has a depth of about 75 μm, whereas the β phase region extends to 150 μm (L5). A similar principle is also applied to calculate the lengths of each region until L5. The present melt pool depth (~75 μm) is close to the calculated depth of ~85 μm in single-track Ti-1Al-8V-

17

5Fe using the Rosenthal equation. The surface temperature was measured by infrared imaging and, subsequently, the melt pool depth was derived by simulations [20]. However, in bulk specimens [39], *in situ* experiments and post-mortem measurements suggest larger melt pool dimensions (500 µm length and 150 µm depth). There are two potential reasons for this difference. First, the 2D nature of a free-standing wall strongly affects heat dissipation, in particular at high temperatures. This will presumably lead to smaller melt pool sizes compared to a bulk specimen. Second, β and liquid phases which are both present in the melt pool tail (layers L1−L3), are difficult to deconvolute in the X-ray spectrum. Therefore, the length and depth of the melt pool measured in this study represent the dimensions of that part of the melt pool that covers the complete thickness of the wall.
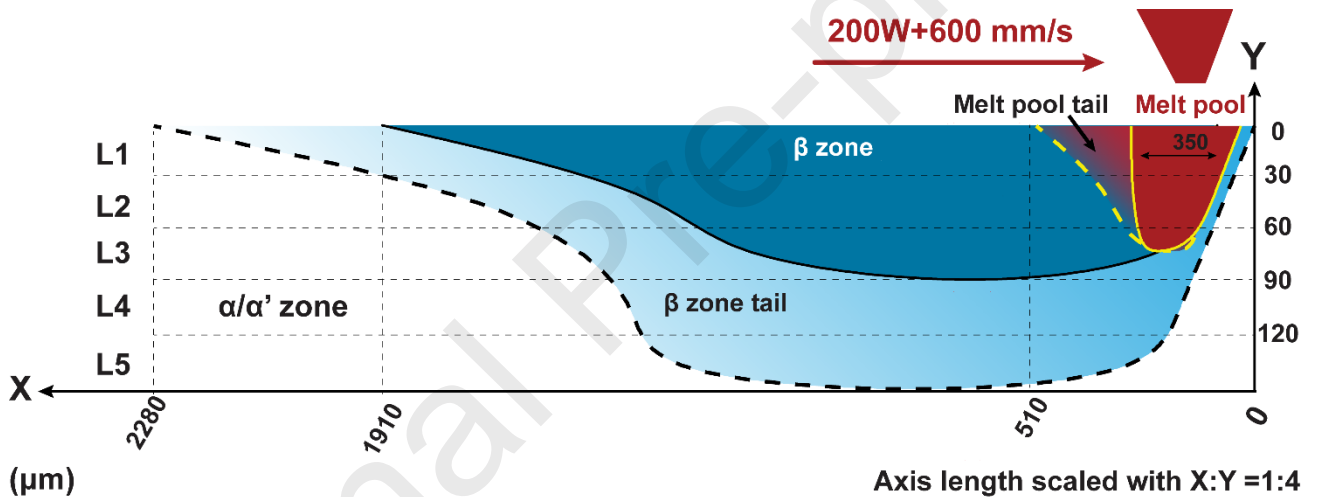

Figure 4. Schematic of the shape of the melt pool (red) and β zone (blue) at the cross-section of the upper layers (L1−L5). The sizes of the melt pool and β zone along the horizontal direction are to scale. The solid line marks a boundary of a zone with a width comparable to the thickness of the wall and the dashed line marks a boundary of the tail part (graded colour) with a width smaller than wall thickness.

4.3 Sources of error in the temperature measurements

There exist several sources that may contribute to the errors in the temperature calculations. Within the V_{XR}, the temperature is not fully homogeneous. Assuming that the HAZ moves at the same speed as the laser, it is possible to provide a rough estimate for the temperature gradients in the direction of the laser motion. For layers

18

L1, L2 and L3, we obtain a maximum gradient of 1.5, 1.2 and 1 K/μm, respectively, when V_{XR} is positioned just next to the melt pool. About 1 mm away from the melt pool, the gradients reduce to 0.1 K/μm. In the building direction, the gradient can be estimated as the derivative of the temperature as a function of depth. Close to the melt pool, we obtain a gradient of 5 K/μm, which reduces to zero at a 1 mm distance from the melt pool. In the direction along with the thickness of the wall (i.e. parallel to the incoming X-ray beam), it is not possible to estimate the temperature gradient. The magnitude of the reported gradients is of the same order as what has been found by FE modelling [6,39].

The rapid heating and cooling cycles during laser scanning induce residual stress in printed Ti-6Al-4V [10]. The residual stress induces lattice strain, changing the position of the diffraction peaks and therefore influencing the temperature calculations. This effect can be estimated by computing the lattice strain from the positions of the {01.1}α/α' and {00.2}α/α' reflections after cooling down to ambient temperatures. All layers exhibit a very small tensile strain with an averaged value of 0.08 ± 0.2%, resulting in an overestimation of the temperature of about 67 ± 24 K. The strain calculated from the {00.2}α/α' reflection is smaller than that from {01.1}α/α', indicating less expansion along *c*-axis of hcp lattice. This can be explained by the larger Young's modulus (~155 GPa) along *c*-axis compared to the other crystalline orientations in the α/α' phase [60]. The higher tensile strains were observed in bulk L-PBF processes Ti-6Al-4V [38,59].

Local fluctuations in the chemical composition may induce changes in the lattice parameters. To verify changes in chemical composition, energy-dispersive X-ray (EDX) measurements were performed on the cross-section of an as-built and a 20x remelted wall. Fig. S9 and Fig. S10 in Supplementary Materials show a homogeneous distribution of Ti, Al and V in both samples. In other words, during the phase transformation, the observed cooling rates of the order of 10^5 K/s are sufficiently high to limit elemental segregation.

4.4 Microstructural evolution of Ti-6Al-4V from L-PBF process

The thermal cycles during L-PBF manufacturing are thought to have a profound effect on the formation and evolution of the hierarchical martensites observed in the printed

Ti-6Al-4V, and primary, secondary, ternary, and quaternary α' laths are typically reported in the literature [24,61]. In Ref [24], Yang et al. proposed a relatively simple process-microstructure model to explain the observed martensite hierarchy. The model predicts that during printing, the first 3−4 layers would reach temperatures above T_β, while the layers below would experience peak temperatures below T_β. This is similar to the results obtained in our study, which are summarised in Fig. 3. Yang et al. also suggest, however, only primary martensite forms immediately after printing (L1) and that at least 4 to 5 thermal cycles are required to form finer secondary, tertiary and quaternary martensites. This is in contrast to that observed in our study. Fig. 5a−5c presents high-resolution EBSD IPF maps of L1, L3, and L7. Several martensitic laths of various thicknesses are already found in L1 a layer that did not experience any thermal cycle. Furthermore, the martensitic structure in L1 is similar to that observed in L3 and L7, layers that were subjected to two and six thermal cycles, respectively.

To gain further insights into the formation of the martensitic structure, an EBSD IPF map of the entire cross-section of the wall (layers L1−L8 are indicated) together with a map depicting the corresponding parent β grains are shown in Fig. 5g and 5h. It is observed that the columnar β grains exhibit a major axis along the build direction [62–64]. The size of the β grains close to the wall surface is smaller than those of the interior grains due to the more rapid cooling. Since α/α' laths can traverse the whole β grain, i.e. the maximum length of α/α' laths is comparable to the width of the primary β grains, it is expected that close to the surface finer α/α' laths with shorter length and narrower width are present. Since the evolution of the martensite variants is not the focus of our experiments, we leave this topic for further research.
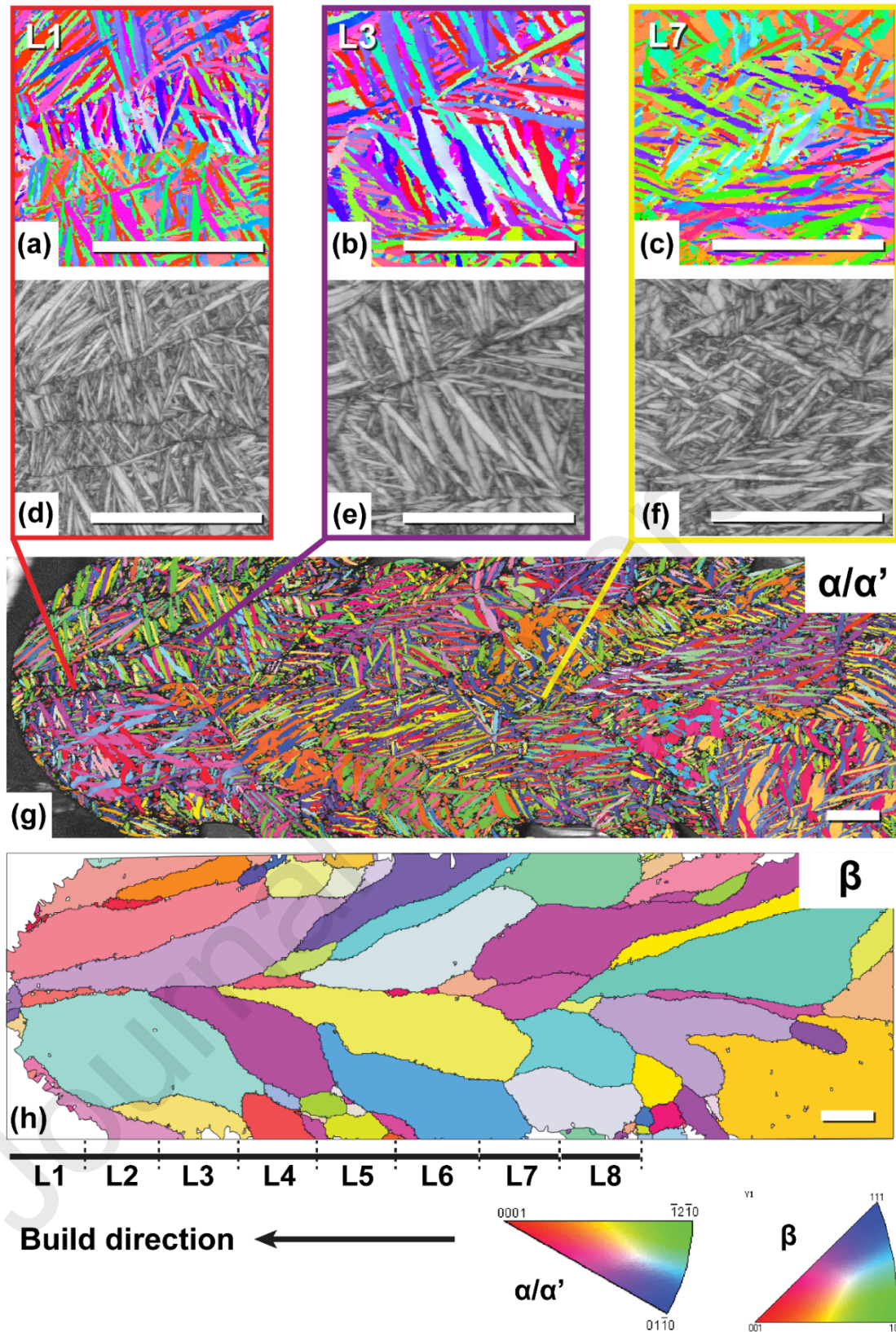
Figure 5. Microstructures of the cross-section at the upper part of Ti-6Al-4V wall in the as-built state from EBSD measurements. High-resolution inverse pole figure maps (a-c) and band contrast images (d-f) of L1, L3, and L7. (g) IPF map of the cross-section

of the whole wall. (h) IPF map of reconstructed primary β grains for the same region. Scale bar: 20 μm.

5. Conclusions

In situ X-ray diffraction has been performed on multiple layers along the build direction of a single-track Ti-6Al-4V wall while laser rescanning on the top layer, providing phase evolution and temperature profiles. The temperatures as a function of time of each layer are used to calculate cooling rates, enabling a quantitative study of thermal cycling during L-PBF manufacturing. The dimensions and shape of the melt pool and β zone in the laser heat-affected zone are estimated. The following conclusions can be drawn:

- The thermal cycles experienced in the first 5 layers (L1−L5), layer thickness 30 μm, reach a maximum temperature exceeding the beta transus temperature of T_β=1252 K. Below a depth of 180 μm under the surface (after layer L6), the peak temperatures of thermal cycles are too low to induce a phase transformation for the applied laser parameters.
- The martensitic start temperatures measured for a thin wall during laser scanning are lower than those reported for conventional manufacturing processes with lower cooling rates, e.g. water quenching.
- The melt pool extends the entire wall thickness in L1 and has approximately a length of 350 μm and a depth of 75 μm. The length and depth are smaller compared to what is observed for bulk specimens, witnessing the importance of radiation loss at the free surfaces.
- The higher cooling rate (~1×10^6 K/s) measured in the top layer of a single-track wall compared to that in bulk structures (~4.6×10^5 K/s) confirms a geometrical effect on the cooling rates. The measured cooling rates vary in a range of 2×10^1−1×10^6 K/s.

It is anticipated that our in situ measurements in transmission on a thin wall, combined with *in situ* measurements in reflection on a bulk sample provide the necessary data to validate FEM models. It should be emphasized that the data of the wall should be compared with FEM simulations of a wall structure since the presence of additional surfaces changes the heat dissipation.

CRediT authorship statement

Ming Chen: Conceptualization, Software, Formal analysis, Investigation, Writing - original draft, Writing - review & editing, Visualization. **Marco Simonelli:** Conceptualization, Validation, Resources, Writing - Review & Editing. **Steven Van Petegem:** Conceptualization, Methodology, Software, Formal analysis, Investigation, Supervision, Writing -review & editing, Visualization. **Yau Yau Tse:** Formal analysis, Resources. **Cynthia Sin Ting Chang:** Investigation. **Malgorzata Grazyna Makowska:** Investigation. **Dario Ferreira Sanchez:** Methodology, Investigation, Resources. **Helena Van Swygenhoven**: Conceptualization, Methodology, Writing - review & editing, Supervision, Project administration, Funding acquisition.

Declaration of Competing Interests

The authors declare that they have no known competing financial interests or personal relationships that could have appeared to influence the work reported in this paper.

Acknowledgement

Data Availability.

Data that support the findings of this report are available from the corresponding author upon request.

References

[1]   T. Vilaro, C. Colin, J.D. Bartout, As-Fabricated and Heat-Treated Microstructures of the Ti-6Al-4V Alloy Processed by Selective Laser Melting, Metall. Mater. Trans. A. 42 (2011) 3190–3199.

[2]   A.A. Antonysamy, J. Meyer, P.B. Prangnell, Effect of build geometry on the β-grain structure and texture in additive manufacture of Ti6Al4V by selective electron beam melting, Mater. Charact. 84 (2013) 153–168.

[3]   J. Goldak, A. Chakravarti, M. Bibby, A new finite element model for welding heat sources, Metall. Trans. B. 15 (1984) 299–305.

[4]   J. Irwin, E.W. Reutzel, P. Michaleris, J. Keist, A.R. Nassar, Predicting Microstructure From Thermal History During Additive Manufacturing for Ti-6Al-4V, J. Manuf. Sci. Eng. 138 (2016) 1–11.

[5]   Q. Zhang, J. Xie, Z. Gao, T. London, D. Griffiths, V. Oancea, A metallurgical phase transformation framework applied to SLM additive manufacturing processes, Mater. Des. 166 (2019) 107618.

[6]   C.H. Fu, Y.B. Guo, Three-Dimensional Temperature Gradient Mechanism in Selective Laser Melting of Ti-6Al-4V, J. Manuf. Sci. Eng. Trans. ASME. 136 (2014) 1–7.

[7]   B. Song, S. Dong, H. Liao, C. Coddet, Process parameter selection for selective laser melting of Ti6Al4V based on temperature distribution simulation and experimental sintering, Int. J. Adv. Manuf. Technol. 61 (2012) 967–974.

[8]   M. V. Pantawane, Y.-H. Ho, S.S. Joshi, N.B. Dahotre, Computational Assessment of Thermokinetics and Associated Microstructural Evolution in Laser Powder Bed Fusion Manufacturing of Ti6Al4V Alloy, Sci. Rep. 10 (2020) 7579.

[9]   M. V. Pantawane, S. Sharma, A. Sharma, S. Dasari, S. Banerjee, R. Banerjee, N.B. Dahotre, Coarsening of martensite with multiple generations of twins in laser additively manufactured Ti6Al4V, Acta Mater. 213 (2021) 116954.

[10]   H. Ali, H. Ghadbeigi, K. Mumtaz, Residual stress development in selective laser-melted Ti6Al4V: a parametric thermal modelling approach, Int. J. Adv. Manuf. Technol. 97 (2018) 2621–2633.

[11]   L. Parry, I.A. Ashcroft, R.D. Wildman, Understanding the effect of laser scan strategy on residual stress in selective laser melting through thermo-mechanical simulation, Addit. Manuf. 12 (2016) 1–15.

[12]   Y. Liu, Y. Yang, D. Wang, A study on the residual stress during selective laser melting (SLM) of metallic powder, Int. J. Adv. Manuf. Technol. 87 (2016) 647–656.

[13]   L.-X. Lu, N. Sridhar, Y.-W. Zhang, Phase field simulation of powder bed-based additive manufacturing, Acta Mater. 144 (2018) 801–809.

[14]   N.H. Paulson, B. Gould, S.J. Wolff, M. Stan, A.C. Greco, Correlations between thermal history and keyhole porosity in laser powder bed fusion, Addit. Manuf. 34 (2020) 101213.

[15]   S. Kelly, S. Kampe, Microstructural Evolution in Laser-Deposited Multilayer Ti-6Al-4V Builds: Part II. Thermal Modeling, Metall. Mater. Trans. A. 35 (2004) 1869–1879.

[16]   T.F. Broderick, A.G. Jackson, H. Jones, F.H. Froes, The effect of cooling conditions on the microstructure of rapidly solidified Ti-6Al-4V, Metall. Trans. A. 16 (1985) 1951–1959.

[17]   T. Ahmed, H.J. Rack, Phase transformations during cooling in α+β titanium alloys, Mater. Sci. Eng. A. 243 (1998) 206–211.

[18]   J. Haubrich, J. Gussone, P. Barriobero-Vila, P. Kürnsteiner, E.A. Jägle, D. Raabe, N. Schell, G. Requena, The role of lattice defects, element partitioning and intrinsic heat effects on the microstructure in selective laser melted Ti-6Al-4V, Acta Mater. 167 (2019) 136–148.

[19]   C.H. Ng, M.J. Bermingham, M.S. Dargusch, Eliminating segregation defects during additive manufacturing of high strength β-titanium alloys, Addit. Manuf. 39 (2021) 101855.

[20]   F.F. Ahmed, S.J. Clark, C.L. Alex Leung, L. Stanger, J. Willmott, S. Marussi, V. Honkimaki, N.

Haynes, H.S. Zurob, P.D. Lee, A.B. Phillion, Achieving homogeneity in a high-Fe β-Ti alloy laser-printed from blended elemental powders, Mater. Des. (2021) 110072.

[21] A. Zafari, M.R. Barati, K. Xia, Controlling martensitic decomposition during selective laser melting to achieve best ductility in high strength Ti-6Al-4V, Mater. Sci. Eng. A. 744 (2019) 445–455.

[22] A. Hadadzadeh, E. Asadi, S. Imam Shakil, B. Shalchi Amirkhiz, M. Mohammadi, M. Haghshenas, Indentation-derived mechanical properties of Ti-6Al-4V: Laser-powder bed fusion versus electron beam melting, Mater. Lett. 301 (2021) 130273.

[23] H. Chandra Kaushik, S.I. Shakil, B.S. Amirkhiz, M. Mohammadi, E. Asadi, M. Haghshenas, A. Hadadzadeh, Indentation strain rate sensitivity of laser-powder bed fused and electron beam melted Ti–6Al–4V, Vacuum. 195 (2022) 110690.

[24] J. Yang, H. Yu, J. Yin, M. Gao, Z. Wang, X. Zeng, Formation and control of martensite in Ti-6Al-4V alloy produced by selective laser melting, Mater. Des. 108 (2016) 308–318.

[25] M. V. Pantawane, S. Dasari, S.A. Mantri, R. Banerjee, N.B. Dahotre, Rapid thermokinetics driven nanoscale vanadium clustering within martensite laths in laser powder bed fused additively manufactured Ti6Al4V, Mater. Res. Lett. 8 (2020) 383–389.

[26] Y. Peng, K. Miao, W. Sun, C. Liu, H. Wu, L. Geng, G. Fan, Recent Progress of Synchrotron X-Ray Imaging and Diffraction on the Solidification and Deformation Behavior of Metallic Materials, Acta Metall. Sin. (English Lett. 35 (2022) 3–24.

[27] C. Zhao, N.D. Parab, X. Li, K. Fezzaa, W. Tan, A.D. Rollett, T. Sun, Critical instability at moving keyhole tip generates porosity in laser melting, Science (80-.). 370 (2020) 1080–1086.

[28] Y. Chen, S.J. Clark, D.M. Collins, S. Marussi, S.A. Hunt, D.M. Fenech, T. Connolley, R.C. Atwood, O. V. Magdysyuk, G.J. Baxter, M.A. Jones, C.L.A. Leung, P.D. Lee, Correlative Synchrotron X-ray Imaging and Diffraction of Directed Energy Deposition Additive Manufacturing, Acta Mater. 209 (2021) 116777.

[29] C.L.A. Leung, S. Marussi, R.C. Atwood, M. Towrie, P.J. Withers, P.D. Lee, In situ X-ray imaging of defect and molten pool dynamics in laser additive manufacturing, Nat. Commun. 9 (2018) 1355.

[30] L. Massimi, S.J. Clark, S. Marussi, A. Doherty, J. Schulz, S. Marathe, C. Rau, M. Endrizzi, P.D. Lee, A. Olivo, Dynamic Multicontrast X-Ray Imaging Method Applied to Additive Manufacturing, Phys. Rev. Lett. 127 (2021) 215503.

[31] H. Ghasemi-Tabasi, C. de Formanoir, S. Van Petegem, J. Jhabvala, S. Hocine, E. Boillat, N. Sohrabi, F. Marone, D. Grolimund, H. Van Swygenhoven, R.E. Logé, Direct observation of crack formation mechanisms with operando Laser Powder Bed Fusion X-ray imaging, Addit. Manuf. (2022) 102619.

[32] J. Epp, J. Dong, H. Meyer, A. Bohlen, Analysis of cyclic phase transformations during additive manufacturing of hardenable tool steel by in-situ X-ray diffraction experiments, Scr. Mater. 177 (2020) 27–31.

[33] F. Schmeiser, E. Krohmer, N. Schell, E. Uhlmann, W. Reimers, Experimental observation of stress formation during selective laser melting using in situ X-ray diffraction, Addit. Manuf. 32 (2020) 101028.

[34] C. Kenel, D. Grolimund, X. Li, E. Panepucci, V.A. Samson, D.F. Sanchez, F. Marone, C. Leinenbach, In situ investigation of phase transformations in Ti-6Al-4V under additive manufacturing conditions combining laser melting and high-speed micro-X-ray diffraction, Sci. Rep. 7 (2017) 1–10.

[35] S.A. Oh, R.E. Lim, J.W. Aroh, A.C. Chuang, B.J. Gould, J. V. Bernier, N. Parab, T. Sun, R.M. Suter, A.D. Rollett, Microscale Observation via High-Speed X-ray Diffraction of Alloy 718 During In Situ Laser Melting, JOM. 73 (2021) 212–222.

[36] C. Zhao, K. Fezzaa, R.W. Cunningham, H. Wen, F. De Carlo, L. Chen, A.D. Rollett, T. Sun, Real-time monitoring of laser powder bed fusion process using high-speed X-ray imaging and diffraction, Sci. Rep. 7 (2017) 3602.

[37]   S.A. Oh, R.E. Lim, J.W. Aroh, A.C. Chuang, B.J. Gould, B. Amin-Ahmadi, J. V. Bernier, T. Sun, P.C. Pistorius, R.M. Suter, A.D. Rollett, High speed synchrotron X-ray diffraction experiments resolve microstructure and phase transformation in laser processed Ti-6Al-4V, Mater. Res. Lett. 9 (2021) 429–436.

[38]   S. Hocine, H. Van Swygenhoven, S. Van Petegem, C.S.T. Chang, T. Maimaitiyili, G. Tinti, D. Ferreira Sanchez, D. Grolimund, N. Casati, Operando X-ray diffraction during laser 3D printing, Mater. Today. 34 (2020) 30–40.

[39]   S. Hocine, H. Van Swygenhoven, S. Van Petegem, Verification of selective laser melting heat source models with operando X-ray diffraction data, Addit. Manuf. 37 (2021) 101747.

[40]   L. Qian, J. Mei, J. Liang, X. Wu, Influence of position and laser power on thermal history and microstructure of direct laser fabricated Ti–6Al–4V samples, Mater. Sci. Technol. 21 (2005) 597–605.

[41]   S. Hocine, S. Van Petegem, U. Frommherz, G. Tinti, N. Casati, D. Grolimund, H. Van Swygenhoven, A miniaturized selective laser melting device for operando X-ray diffraction studies, Addit. Manuf. 34 (2020) 101194.

[42]   G. Tinti, A. Bergamaschi, S. Cartier, R. Dinapoli, D. Greiffenberg, I. Johnson, J.H. Jungmann-Smith, D. Mezza, A. Mozzanica, B. Schmitt, X. Shi, Performance of the EIGER single photon counting detector, J. Instrum. 10 (2015) C03011.

[43]   G. Ashiotis, A. Deschildre, Z. Nawaz, J.P. Wright, D. Karkoulis, F.E. Picca, J. Kieffer, The fast azimuthal integration Python library: pyFAI, J. Appl. Crystallogr. 48 (2015) 510–519.

[44]   P. Fischer, V. Romano, H.P. Weber, N.P. Karapatis, E. Boillat, R. Glardon, Sintering of commercially pure titanium powder with a Nd:YAG laser source, Acta Mater. 51 (2003) 1651–1662.

[45]   M.F. Modest, J. Ready, D. Farson, Handbook of laser materials processing, (2001).

[46]   M. Keller, A. Chaudhary, S. Kelly, S. Medieros, Absorption coefficient characterization in Ti-6Al-4V laser additive manufacturing, in: Int. Congr. Appl. Lasers Electro-Optics, Laser Institute of America, 2006: p. 1204.

[47]   R.P. Martukanitz, R.M. Melnychuk, M.S. Stefanski, S.M. Copley, Dynamic absorption of a powder layer, in: Int. Congr. Appl. Lasers Electro-Optics, Laser Institute of America, 2004: p. 1404.

[48]   X. Tan, Y. Kok, W.Q. Toh, Y.J. Tan, M. Descoins, D. Mangelinck, S.B. Tor, K.F. Leong, C.K. Chua, Revealing martensitic transformation and α/β interface evolution in electron beam melting three-dimensional-printed Ti-6Al-4V, Sci. Rep. 6 (2016) 26039.

[49]   B.D. Cullity, Elements of X-ray diffraction, Third Edit, Pearson Education Limited, 2014.

[50]   J.W. Elmer, T.A. Palmer, S.S. Babu, E.D. Specht, In situ observations of lattice expansion and transformation rates of α and β phases in Ti-6Al-4V, Mater. Sci. Eng. A. 391 (2005) 104–113.

[51]   Y.S. Touloukian, R.K. Kirby, R.E. Taylor, P.D. Desai, Thermal Expansion, Springer US, Boston, MA, 1975.

[52]   A. Ducato, L. Fratini, M. La Cascia, G. Mazzola, An Automated Visual Inspection System for the Classification of the Phases of Ti-6Al-4V Titanium Alloy, in: R. Wilson, E. Hancock, A. Bors, W. Smith (Eds.), Comput. Anal. Images Patterns, Springer Berlin Heidelberg, Berlin, Heidelberg, 2013: pp. 362–369.

[53]   S.L. Lu, M. Qian, H.P. Tang, M. Yan, J. Wang, D.H. StJohn, Massive transformation in Ti–6Al–4V additively manufactured by selective electron beam melting, Acta Mater. 104 (2016) 303–311.

[54]   M. Masoomi, J.W. Pegues, S.M. Thompson, N. Shamsaei, A numerical and experimental investigation of convective heat transfer during laser-powder bed fusion, Addit. Manuf. 22 (2018) 729–745.

[55]   M. Chiumenti, E. Neiva, E. Salsi, M. Cervera, S. Badia, J. Moya, Z. Chen, C. Lee, C. Davies, Numerical modelling and experimental validation in Selective Laser Melting, Addit. Manuf. 18 (2017) 171–185.

[56] T. DebRoy, H.L. Wei, J.S. Zuback, T. Mukherjee, J.W. Elmer, J.O. Milewski, A.M. Beese, A. Wilson-Heid, A. De, W. Zhang, Additive manufacturing of metallic components – Process, structure and properties, Prog. Mater. Sci. 92 (2018) 112–224.

[57] S.Y. Choy, C.-N. Sun, K.F. Leong, J. Wei, Compressive properties of Ti-6Al-4V lattice structures fabricated by selective laser melting: Design, orientation and density, Addit. Manuf. 16 (2017) 213–224.

[58] C. de Formanoir, G. Martin, F. Prima, S.Y.P. Allain, T. Dessolier, F. Sun, S. Vivès, B. Hary, Y. Bréchet, S. Godet, Micromechanical behavior and thermal stability of a dual-phase α+α' titanium alloy produced by additive manufacturing, Acta Mater. 162 (2019) 149–162.

[59] V. Thampy, A.Y. Fong, N.P. Calta, J. Wang, A.A. Martin, P.J. Depond, A.M. Kiss, G. Guss, Q. Xing, R.T. Ott, A. van Buuren, M.F. Toney, J.N. Weker, M.J. Kramer, M.J. Matthews, C.J. Tassone, K.H. Stone, Subsurface Cooling Rates and Microstructural Response during Laser Based Metal Additive Manufacturing, Sci. Rep. 10 (2020) 1–9.

[60] N. Dumontet, D. Connétable, B. Malard, B. Viguier, Elastic properties of the α' martensitic phase in the Ti-6Al-4V alloy obtained by additive manufacturing, Scr. Mater. 167 (2019) 115–119.

[61] M. Muhammad, M. Masoomi, B. Torries, N. Shamsaei, M. Haghshenas, Depth-sensing time-dependent response of additively manufactured Ti-6Al-4V alloy, Addit. Manuf. 24 (2018) 37–46.

[62] L. Thijs, F. Verhaeghe, T. Craeghs, J. Van Humbeeck, J.P. Kruth, A study of the microstructural evolution during selective laser melting of Ti-6Al-4V, Acta Mater. 58 (2010) 3303–3312.

[63] M. Simonelli, Y.Y. Tse, C. Tuck, Effect of the build orientation on the mechanical properties and fracture modes of SLM Ti–6Al–4V, Mater. Sci. Eng. A. 616 (2014) 1–11.

[64] A. Soltani-Tehrani, M. Habibnejad-Korayem, S. Shao, M. Haghshenas, N. Shamsaei, Ti-6Al-4V powder characteristics in laser powder bed fusion: The effect on tensile and fatigue behavior, Addit. Manuf. 51 (2022) 102584.
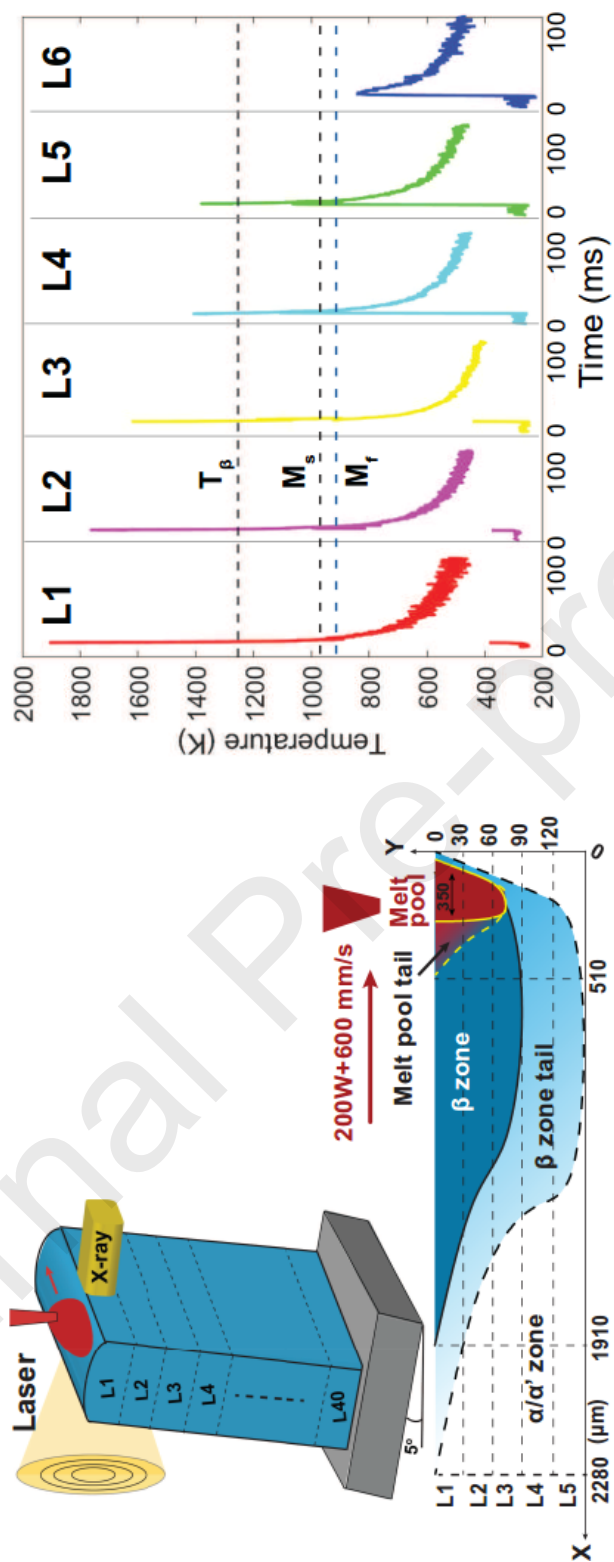
Highlights

- High-speed *in situ* X-ray diffraction during laser scanning were performed on a Ti-6Al-4V thin wall produced by laser powder bed fusion.
- The temperature evolution and cooling rates were determined as a function of depth with a time resolution of 50μs
- Based on the evolution of the crystallographic phases the shape of the melt pool and the β phase in the heat-affected zone could be estimated
- The depth-dependent temperature profiles provide valuable input for the calibration of finite element simulations

Declaration of interests

x The authors declare that they have no known competing financial interests or personal relationships that could have appeared to influence the work reported in this paper.

☐ The authors declare the following financial interests/personal relationships which may be considered as potential competing interests:

Graphical Abstract

Declaration of interests

x The authors declare that they have no known competing financial interests or personal relationships that could have appeared to influence the work reported in this paper.

☐ The authors declare the following financial interests/personal relationships which may be considered as potential competing interests: